GLOBAL-SCALE *P*-WAVE TOMOGRAPHY DESIGNED FOR ACCURATE PREDICTION OF REGIONAL AND TELESEISMIC TRAVEL TIMES FOR MIDDLE EAST EVENTS

Nathan A. Simmons, Stephen C. Myers, and Gardar Johannesson

Lawrence Livermore National Laboratory

Sponsored by the National Nuclear Security Administration

Award No. DE-AC52-07NA27344/LL09-3Dseismic-NDD02

ABSTRACT

A global-scale *P*-wave tomography model of the crust and mantle is constructed. The model depicts both large-scale tectonic/dynamic features, as well as detailed upper mantle heterogeneities beneath the greater Middle East region. Fully three-dimensional ray tracing is employed to achieve accurate travel-time predictions of a suite of *P* and P_n arrivals, necessitating the characterization of irregular and discontinuous boundaries. Therefore, we explicitly represent undulating seismic discontinuities in the crust and upper mantle within a spherical tessellation modeling framework. The tessellation-based model architecture is hierarchical in that fine node sampling is achieved by recursively subdividing a base-level tessellation. Determining the required node spacing to effectively model a given set of data is problematic, given the uneven sampling of seismic data and the differing wavelengths of actual seismic heterogeneity. To address this problem, we have developed an inversion process called *Progressive Multi-level Tessellation Inversion* (PMTI) that exploits the hierarchical nature of the tessellation-based design and is well-suited for modeling a mixture of teleseismic and regional data. PMTI allows the data to determine the level of model complexity by progressively solving for shorter wavelength structure, thereby robustly imaging regional trends and allowing localized details to emerge where resolution is sufficient. Using the PMTI approach, we have developed a global-scale *P*-wave model that simultaneously predicts teleseismic *P* and P_n travel times for events occurring throughout the Middle East. The tomographic image provides a new glimpse of the complex upper mantle velocity anomalies associated with the convergence of the Arabian and Indian plates with Eurasia along the Tethyan margin.

OBJECTIVES

Travel time predictions based on global tomography models can improve seismic event location accuracy (e.g., Antolik et al. 2001, 2003). However, *P*-wave models, derived from teleseismic data, lack detailed structures in the upper mantle and generally do not accurately predict regional travel times as a result. Regional-scale models of upper mantle P-wave velocity structure are therefore essential for locating small seismic events. Detailed upper mantle P-wave velocities may be interpreted from surface wave solutions with some success (e.g., Ritzwoller et al. 2003); however these solutions are not specifically optimized for the prediction of P_n travel times. Additionally, hybrid combinations of independent regional and teleseismic models tend to be inconsistent since the predicted teleseismic (i.e., *P*) and regional (i.e., P_n) travel times often conflict (Yang et al. 2004). At a minimum, baseline travel time shifts must be determined through the calculation of travel time correction surfaces in order to reduce the 1st-order regional-teleseismic travel time inconsistencies generated by the hybrid models.

The objective of this project is to further advance event monitoring capabilities, through the generation of a seamless model of the Earth's crust and mantle that is capable of self-consistently predicting regional and teleseismic travel times as accurately as possible. Effectively, this requires simultaneous modeling of detailed upper mantle heterogeneities to adequately predict regional phases such as P_n and lower mantle structures to predict teleseismic travel times. It is also highly desirable to develop a model and techniques that reduce the need for numerous travel time corrections (e.g., crustal corrections, Earth's ellipticity, etc.) and/or massive travel time lookup tables. In this report, we present our progress toward the development of a global 3-D seismic event monitoring model.

RESEARCH ACCOMPLISHED

We have established a set of global 3-D tomographic model design components and procedures including a statistical event location/data culling process and a novel inversion technique that is specifically designed to exploit the hierarchical nature of our tessellation-based model representation. We apply our modeling procedures to produce a global-scale model of *P*-wave velocity structure based upon *P* and P_n travel times from >4,000 Middle East events and an additional ~1,000 globally-distributed seismic events. The new tomographic image contains large-scale features seen in most modern global tomographic models, but also contains previously un-imaged details of the Arabia plate beneath Eurasia. The model is consistent with geology and predicts >800,000 *P* and P_n travel times to with 0.53 seconds standard deviation when statistics-based data corrections are considered.

Model Representation and Inversion Technique

Our model parameterization is based on triangular tessellations of a spherical surface. Spherical tessellation parameterizations have been employed for multiple geophysical applications including mantle convection simulations (Baumgardner and Frederickson 1985), magnetic field modeling (Constable et al. 1993), and the basis for representation of Earth's seismic velocity structure (e.g., Wang and Dahlen 1995; Chiao and Kuo 2001; Ishii and Dziewonski 2002; Ballard et al. 2009; Myers et al. 2010). The primary purpose for employing spherical tessellations is to generate a mesh of nearly evenly spaced nodes (or knots), therefore preventing the polar distortion effects of a latitude-longitude grid. Building a spherical tessellation mesh involves recursive subdivision of triangular facets of an initial polyhedron (in our case, an icosahedron) into smaller sub-triangles whose vertices are projected onto a unit sphere (Figure 1). Each sub-division of a triangular facet ('*parent*') produces 4 triangular facets ('*daughters*') and thus increases the number of nearly evenly spaced vertices. We refer to each tessellation recursion as a '*Level*' starting with the initial object (Level 1; Figure 1) up to Level *N*, where *N* is some maximum recursion level. For example, a Level 7 recursion results in node spacing of approximately 1° when an icosahedron is used as the initial object. Although the tessellation meshes represent simple sphere-like surfaces, they form the basis of an aspherical Earth representation in this study. See Ballard et al. (2008, 2009) and Simmons et al. (2009) for more information on the model design and communication.

The tomographic imaging procedure developed for this project, PMTI, is designed with the same underlying philosophy as the wavelet and multi-grid approaches described in Chiao and Kuo (2001) and Zhou (1996), respectively. Specifically, the PMTI technique circumvents the need for predefining variable resolution scales through the hierarchical expression of higher resolution solutions as perturbations to lower resolution models. The most notable difference of PMTI from the wavelet and multi-grid approaches is that model components are found *progressively* through inversions of tomographic systems built upon successively finer parameterizations defined by

a hierarchy of tessellation grids. Therefore, multiple parameter grids with different node densities are not considered simultaneously and wavelet transforms are unnecessary. Each successive model component is added to the previous solution to form a total model field. As with the wavelet and multi-grid approaches, the data drive the resulting variable resolution scales and finer detail structures emerge from the regional trends only where it is necessary to explain the given set of observations. The PMTI process is described at a high level by the following algorithm:

$$\mathbf{x}_1 = \mathbf{A}_1^{-1}\mathbf{b}$$
$$\mathbf{b}_1 = \mathbf{b} - \mathbf{A}_1\mathbf{x}_1$$
$$for\ i = 2 \ldots N$$
$$\mathbf{x}_i = \mathbf{x}_{i-1}^{*} + \mathbf{A}_i^{-1}\mathbf{b}_{i-1}$$
$$\mathbf{b}_i = \mathbf{b} - \mathbf{A}_i\mathbf{x}_i$$
$$end$$

Beginning with the initial travel time residuals ($\mathbf{b}$) and sensitivity kernels defined at the lowest resolution level ($\mathbf{A}_1$), an initial slowness perturbation model ($\mathbf{x}_1$) is determined through an inversion process. The initial travel time residuals are subsequently reduced by the residuals predicted by the lowest-resolution solution to produce a new data vector, $\mathbf{b}_1$. An inversion is then performed on the basis of sensitivity kernels defined at the next resolution level ($\mathbf{A}_2$) and the reduced data vector ($\mathbf{b}_1$). The total slowness perturbation model ($\mathbf{x}_2$) accumulates by summing the interpolated model from the previous step ($\mathbf{x}_1^*$) and the higher resolution solution based on the remaining travel time signals ($\mathbf{A}_2^{-1}\mathbf{b}_1$). All subsequent inversions operate on data vectors reduced by the previous solution ($\mathbf{b}_{i-1}$) to produce slowness perturbations relative to the previous model. Therefore, if a low-resolution solution accounts for all of the travel time signal, the total slowness model ceases to accumulate additional slowness perturbations.

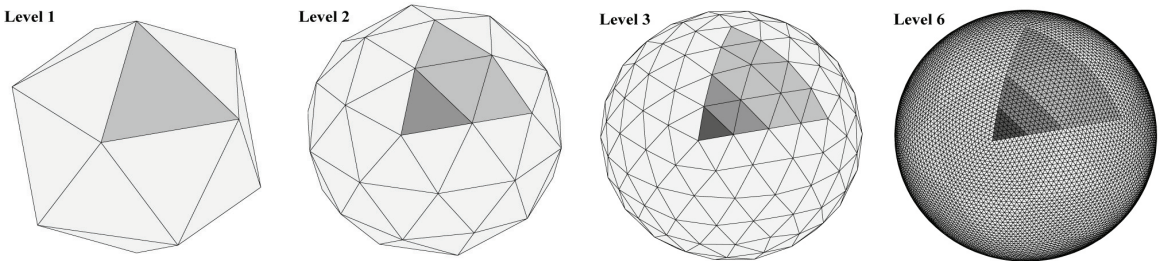

Figure 1. Spherical tessellation grids and parent-daughter triangle relationships. The initial object (a regular icosahedron; Level 1) consists of 20 triangular faces and 12 distinct vertices. The triangular faces (parents) are recursively subdivided into smaller triangles (daughters) and the vertices are normalized to the unit sphere. Each recursion represents a level in the tessellation hierarchy and parent-daughter triangle relationships are indexed for efficient communication. Triangular regions are shaded simply for visual orientation of the parent-daughter regions and sub-regions.

To evaluate the behavior of the PMTI approach, we devised a 3-D synthetic test bed to explore the intricacies of the imaging procedure. The synthetic model domain consists of 3 triangular depth slices with nodes defined by a tessellation procedure up to the Level 5 (Figure 2). We chose to mimic complex, sub-crustal *P* -wave velocity structure with two dominant characteristic wavelengths. Specifically, the synthetic model consists of a long-wavelength regional velocity trend with short-wavelength details embedded within the center of model domain (Figure 2, left). The chosen ray path configuration consisted of clusters of regional phases (sub-lateral travel direction) and teleseismic paths (near vertical travel direction). The ray path density is highly heterogeneous and random noise was added to imitate a realistic shallow mantle imaging problem.

Inversions were performed directly (simple least-squares at the highest tessellation level) and with the PMTI procedure for comparison. A representative solution from a single realization (paths shown in Figure 2 and 20% RMS noise added) is shown in Figure 3. For the simple (or direct) inversion, we incorporated damping and smoothing operators independently and optimized the regularization weights to find the solutions closest to the known solution (based on RMS model misfit). With damping alone, detailed structures emerge where there are a large number of crossing paths (Figure 3; SIMPLE damping). However, instead of recovering the long-wavelength

regional trend, isolated velocity structures are generated without a smooth transition through unresolved regions. In regions with only near-vertical paths (teleseismic phases), circular velocity structures are generated since there is no sensitivity to surrounding nodes. In regions with only bundles of sub-horizontal paths (regional phases), linear velocity anomalies are evident. Such isolated velocity blobs and streaks are undesirable since they may result in geological misinterpretations and also pose serious problems when computing travel times with 3-D ray paths. Alternatively, simple inversion with a first-order smoothing operator (with an optimum weight) recovers the long-wavelength regional trend, but fails to recover fine details where information is sufficient (Figure 7; SIMPLE smoothing). This smooth solution is also undesirable since we would prefer to take full advantage of the resolvability of dense data packets.

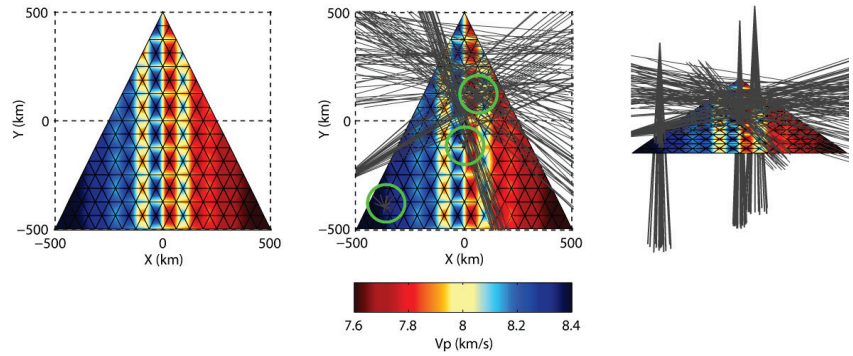

Figure 2. Synthetic tomography scenario imitating a combination of regional and teleseismic phases and complex shallow upper mantle velocity structure parameterized by a triangular tessellation with 5 hierarchical levels. (left) Synthesized velocity structure with a regional trend (from left to right) and embedded, small-scale velocity heterogeneities. (center) Map view of synthetic ray path coverage consisting of several clusters of sub-horizontal regional phase ray paths and 3 clusters of near-vertical teleseismic ray paths (highlighted with green circles). (right) 3-D view of the synthesized ray path coverage.

Using the PMTI approach, the long-wavelength velocity structure is established with the first inversion based on nodes defined by the first level tessellation (Figure 3; PMTI Level 1). Note that only simple damping is used as regularization. The Levels 2-4 PMTI solutions adjust the model only slightly, relative to the Level 1 solution. The minor model variation provided by these intermediate steps is due to the synthetic velocity model design with only two dominant characteristic wavelengths. In the final PMTI stage (Level 5 inversion), detailed structures emerge from the underlying long-wavelength velocity trend (Figure 3; PMTI Level 5). The detailed anomalies are most refined where data coverage is dense and ray path travel directions are diverse. It should be noted that the slight changes through the first 3 progressions demonstrates the potential pitfalls of an alternative imaging procedure involving dynamic mesh refinement (e.g., Sambridge and Faletič 2003). A dynamic mesh refinement procedure would likely cease to insert new model nodes, thereby never recovering the fine (yet resolvable) details. Our tests also reveal that the PMTI solution is less dependent on the choice of damping weight than a simple direct inversion. While it is true that a similar model could be recovered through a simple inversion with combined damping *and* smoothing, regularization weights would need to be fine-tuned in order to best match the known solution. In a real scenario, however, the 'true' solution is never known.

The PMTI approach has important advantages over other inversion techniques, especially when considering extreme spatial resolvability variations. If the travel time observations cannot be explained by a long-wavelength velocity trend in a particular region, detailed anomalies emerge from the background velocity model. Therefore, the 'resolution level' is predicated by the data without any user intervention. Dynamic mesh refinement (or adaptive meshing) is one such method of intervention whereby the addition or subtraction of model parameters occurs based on some user-defined criteria, thus generating an irregular grid. Aside from the additional complexity of establishing and communicating with a model based on an irregular grid, our synthetic example demonstrates other potential pitfalls of a dynamic/adaptive mesh refinement approach (Figure 3). For example, if we chose to refine the mesh from one inversion step to the next based on model movement, the imaging process would cease after the inversion based on the nodes defined by the Level 2 triangular tessellation (see Figure 3). This cessation could be prevented through knowledge of the data density (e.g., hit count criteria). However, hit count does not necessarily reflect resolvability since ray paths are commonly bundled providing limited additional constraints on lateral velocity

variations. For ultra-high resolution modeling with a global basis (<0.5° node spacing), adaptive meshing may be required to limit the size of the tomographic systems of equations. For our initial global model design however, we find that irregular meshing is unnecessary.

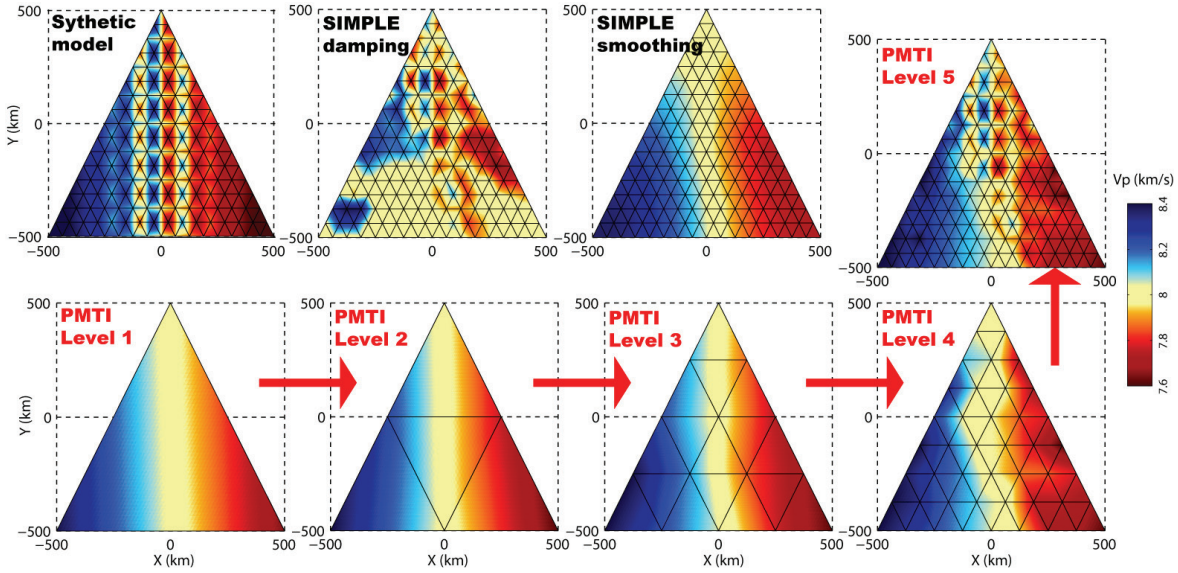

Figure 3. Representative tomography solutions for the synthetic tomography scenario shown in Figure 2. (top row) Synthetic model and 3 possible solutions using different approaches and regularization. With simple inversion and damping ('SIMPLE damping'), detailed structures emerge where there are sufficient crossing paths and isolated velocity structures are generated where there are gaps in ray path coverage. Simple inversion with a first-order smoothing operator ('SIMPLE smoothing') recovers the long-wavelength regional trend, but fails to recover fine details. Using the PMTI approach ('PMTI Level 5'), the regional trend is recovered and details emerge where there is sufficient ray path coverage (in the northern portion of the model space). (bottom row) The accumulation of velocity structure through the PMTI process.

Travel Time Data and Event Locations

We compiled a Middle East-centric set of teleseismic *P* and regional P_n travel time measurements from a subset of our local database at Lawrence Livermore National Laboratory (Ruppert et al. 2005) and the publicly available Engdahl-van der Hilst-Buland (EHB) catalog (Engdahl et al. 1998). The data selection criteria were: 1) all available *P* and P_n travel time measurements from seismic events occurring within the greater Middle East region, and 2) teleseismic *P* measurements from globally distributed events with the largest number of recordings within 5° lateral bins and 7 depth bins from the surface to 700 km depth. In total, we consider 5,401 events (~4,000 within the Middle East) recorded at approximately 4,500 seismic stations around the globe. The data consist of ~800,000 *P* arrivals from globally distributed events and stations, and ~43,000 P_n arrivals to stations within the Middle East (Figure 4). Although the compiled dataset is global in extent, more than 60% of the data are from events occurring within the Middle East and/or arrivals to one of the 600+ seismic stations within the region. Ray path hitcount calculations reveal that most of the shallow upper mantle in the Middle East region is sampled by more than 1,000 *P* and 100 P_n paths providing excellent constraints on detailed velocity structure (Figure 4).

We adapted a multi-event location algorithm, initially designed to simultaneously locate event clusters, to handle a global distribution of seismic events (Myers et al. 2007, 2009). The algorithm, called *BayesLoc*, is a multi-event location algorithm that operates within a hierarchical Bayesian statistical framework. The process entails generating numerous realizations of event hypocenters, origin times, phase labels, and travel time curves using a Markov Chain Monte Carlo (MCMC) sampling scheme. Using prior statistical models, the process allows for complete statistical characterization of the multi-event problem and thus develops a joint posterior distribution of all elements involved. The *BayesLoc* algorithm simultaneously determines event location probability regions, identifies likely outlier arrival time data (inconsistent with the total population), re-labels misidentified seismic phases, and adjusts travel

times based on statistically likelihood. The net result of the procedure is a set of event locations and travel times such that the spread of the travel time residuals relative to the 1-D AK135 (Kennett et al. 1995) velocity model is minimal (Figure 5).

In terms of data variance, the apparent travel time residual signal of the raw data (based on the original event locations) is ~12 times larger than the signal based on the *BayesLoc* event locations. This suggests that a tremendous amount of the apparent signal associated with the raw event locations is not due to 3-D velocity structure, but rather hypocenter mis-location, mis-identified seismic phases and arrival time pick errors. The total signal reduction signifies the improved data consistency that *BayesLoc* provides, but another important aspect is the shift of the mean from a positive 0.44 seconds to a negative 0.53 seconds. This mean shift and the residual trend with distance (see Figure 5) have tremendous implications on the absolute velocity structure needed to explain the data. Hypocenter locations based on single-event location procedures often do not recover such trends; particularly when assuming a location such that the residual travel times are zero-mean.

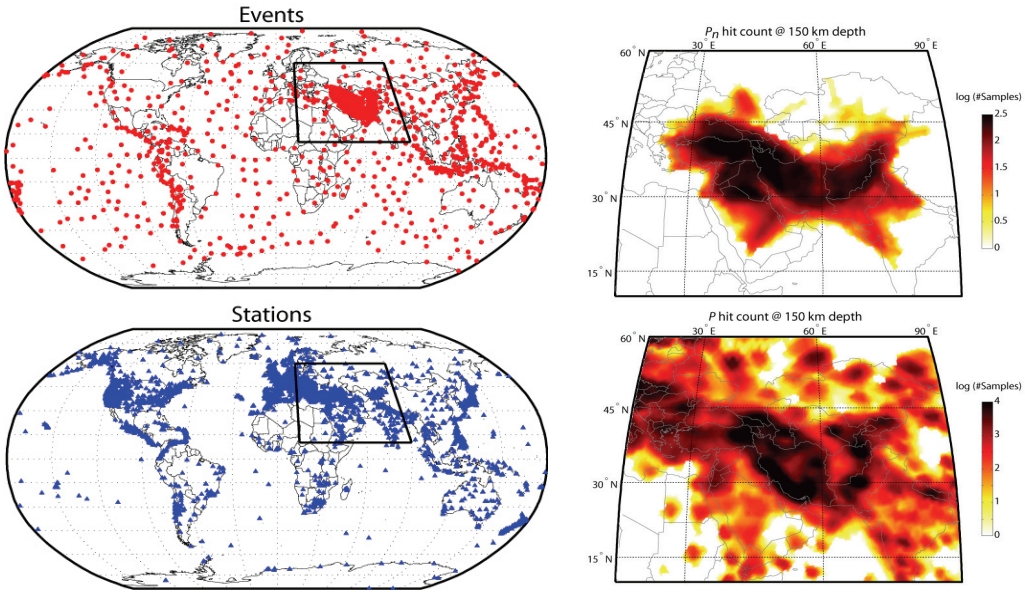

Figure 4. (left column) Selected seismic events (5,401) and stations (4,500) around the globe. (right column) P_n and teleseismic *P* hitcount in the outlined region at a depth of 150 km.

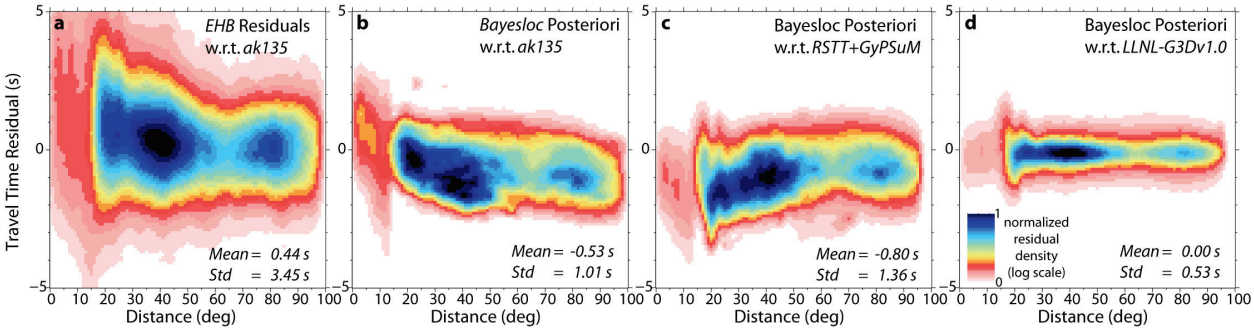

Figure 5. Travel time residuals for the compiled *P* and P_n data set. Residual travel times are plotted as a function of great circle distance in terms of point density on a normalized log scale. (a) Travel time residuals for the initial EHB bulletin and LLNL data set with respect to (w.r.t.) the AK135 1-D velocity model. (b) Travel time residuals w.r.t. AK135 after *BayesLoc* processing. (c) Residuals based on *BayesLoc* processed data relative to the hybrid regional-teleseismic velocity model described in the text (RSTT+GyPSuM). (d) Travel time residuals w.r.t. to the global 3-D *P* wave model constructed in this study (*LLNL-G3Dv1.0*).

3-D Ray Tracing and Sensitivity Definitions

We have adapted a 3-D ray tracing procedure specifically tailored to communicate with the aforementioned tessellation-based model design. The general approach we have taken is based on the techniques originally conceived by Zhao et al. (1992) to model direct arrivals within a subduction zone and extended to teleseismic phases by Zhao and Lei (2004). The procedure combines pseudo-bending in continuous media (Um and Thurber 1987) while simultaneously satisfying Snell's Law at discontinuous interfaces through an iterative process. One major shortcoming of this general approach is the inability to find global minimum travel times and paths for complex regional phases such as P_n. We have therefore adapted the procedure to find such global minima by considering multiple starting ray path configurations. A similar adaptation has recently been developed by Ballard et al. (2009) where the computational process was designed within a distributed computing environment.

In our specific approach, we initially create several crude 3-D ray path estimates based on an imposed set of rules for a given source-receiver configuration. Each of the initial paths is perturbed with a limited set of pseudo-bending iterations and discontinuity piercing point adjustments as described in Zhao et al. (1992). Rather than performing ray path adjustment iterations until convergence, we cull out paths that provide travel times within some tolerance of the minimum time achieved by the full set of perturbed paths (we chose a 1 second tolerance). Ray path adjustment iterations are then performed on the remaining paths until the minimum travel time is attained. The paths that generate the minimum time within a secondary time tolerance (we chose 0.2 seconds) are accepted and used in the development of model space sensitivity kernels. For example, near the upper mantle transition zone crossover distance range (~18° distance for a surface event), ray paths traveling through the shallow upper mantle and below transition zone discontinuities are accepted if they satisfy the minimum time tolerance criterion. By accepting all paths that produce near-minimum travel times, we directly address the multi-pathing problem. Additionally, model sensitivity may be distributed over a wide depth range as opposed to two (or more) distinct geological units in a pure multi-pathing scenario (see the example in Figure 6). Thus, the issue of interdependence of velocity structure and ray path is mitigated.

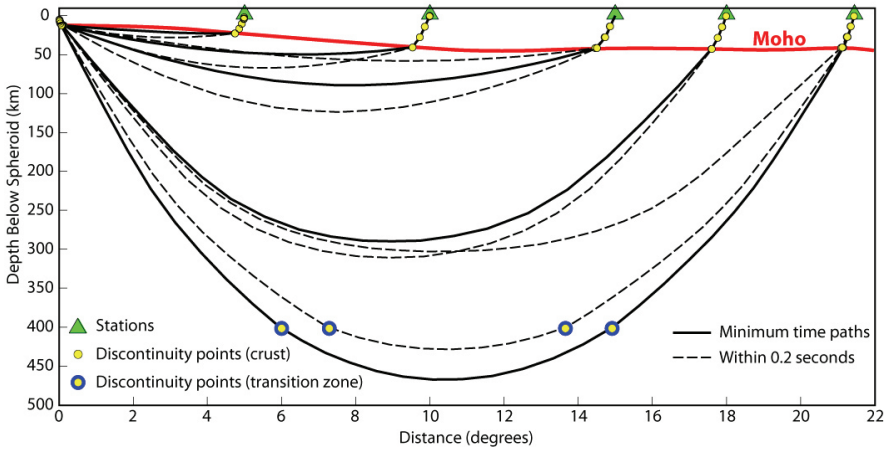

Figure 6. Example 3-D ray paths calculated through the global velocity model constructed in this study. Sensitivity is spread across broad depth zones and/or multiple model units to mitigate the problem of interdependence of paths and velocity structure as well as multi-pathing.

Inversion Procedures and Results

We designed a starting model by combining the Regional Seismic Travel Time (RSTT) model (Myers et al. 2010) and the global joint seismic-geodynamic image called GyPSuM (Simmons et al. 2010). The crust and upper mantle velocity model is represented by 33 layers (including 7 crustal units) with a lateral spacing of ~1° (Level 7 tessellation) and the lower mantle is represented by 25 layers with a lateral spacing of ~2° (Level 6 tessellation). In total, the crust and mantle *P*-wave velocity structure is defined at ~1.6 million points (1.35 million points in the crust and upper mantle; 250,000 points in the lower mantle). Sensitivities to each of the model nodes defined in the starting solution (RSTT+GyPSuM) were determined based on the calculated 3-D ray paths and model space sensitivity definitions described in the previous section. For the inverse problem, we chose to combine certain layers

to limit the number of free parameters and account for limited resolvability in particular depth zones. Specifically, sensitivities to all nodes representing the crust (as defined in the full hybrid model) were summed along the geocentric vertices to define a single set of sensitivity kernels associated with the crust. Therefore, tomographic inversion results in slowness perturbation updates for the entire crustal stack at each lateral position instead of determining model updates within each individual crustal layer. The upper mantle sensitivities were condensed in a similar fashion creating 9 total inversion layers in the crust and upper mantle with an average depth spacing of ~80 km. The lower mantle sensitivities were only slightly condensed providing an average depth spacing of just over 100 km. In total, the node sensitivities defined for the starting model were condensed from 55 model layers and ~1.6 million nodes to 31 layers and ~600,000 free parameters to be determined in the tomographic inversion process.

Global-scale velocity model updates were determined by carrying out the PMTI procedure where successive inversions were performed using the LSQR algorithm (Paige and Saunders 1984). We initiated the progression by solving for model updates at nodes defined by tessellation Level 4 vertices (~8° lateral node spacing) followed by Levels 5,6 and 7 (4°, 2° and 1° node spacing, respectively). We chose not to begin the progressive inversion below Level 4 to limit structural leakage across drastically different tectonic environments. In addition, we chose not to adjust the depth resolution during the progression. A global damping operator was employed as regularization and the damping weight was chosen based on the trade-off of model norm and data misfit (L-curve analysis).

Owing to the substantial non-linearity of ray paths and velocity structure for regional phases, P_n ray paths and sensitivity kernels were re-computed after one complete PMTI cycle and the inversion procedure was performed again. After the 2nd inversion cycle, P_n ray paths were computed once again to test for convergence. It was concluded that most minimum-time ray paths did not change appreciably; and paths that noticeably changed, did not generate substantially different travel time predictions relative to the previous stage. It is our conclusion that the sensitivity definitions, which include multi-pathing and broadened kernels, mitigate the non-linear path-velocity interdependence issues to a large degree. However, we are cautious about generalizing this observation to every scenario and region.

The final *P* -wave model, *LLNL-G3Dv1.0*, predicts the *BayesLoc* posteriori data to within 0.53 seconds standard deviation (Figure 5). This equates to ~72% variance reduction relative to *BayesLoc* posteriori travel times predicted with AK135 (1.01 second standard deviation). The initial bulletin data (without *BayesLoc* statistical operations) are predicted to within 3.45 seconds standard deviation on the basis of the 1-D AK135 Earth model. The combination of *BayesLoc* processing and the *LLNL-G3Dv1.0* velocity model yields data fits on the order of 97% variance reduction relative to the initial data and AK135 (see Figure 5). Thus, the travel times for the ~800,000 *P* and ~43,000 P_n arrivals are predicted to extremely high degrees given the statistical corrections provided by *BayesLoc* and the 3-D velocity heterogeneities in the new global-scale tomographic model shown in Figures 7 and 8.

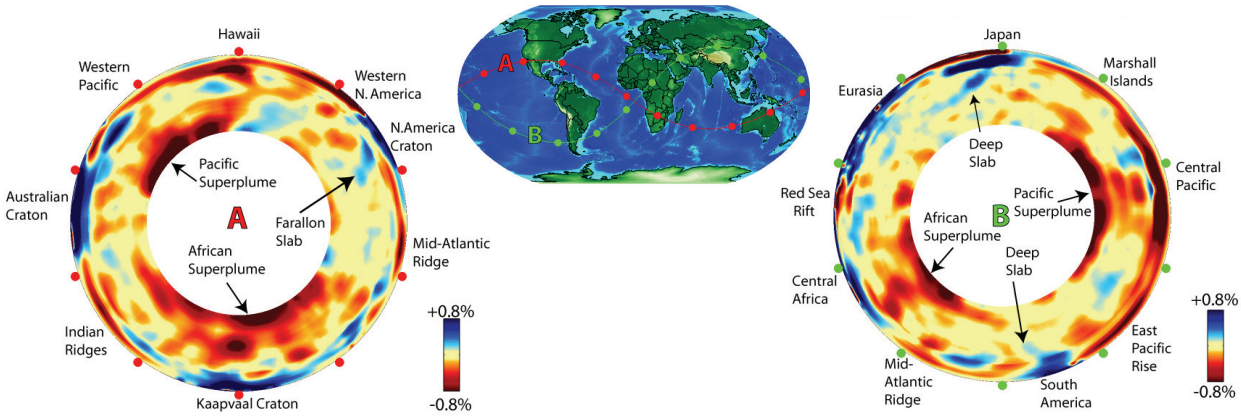

Figure 7. Selected 360° cross sections through the *LLNL-G3Dv1.0* velocity model. Most of the major features highlighted are also observed in the hybrid starting model based on the joint seismic-geodynamic image called GyPSuM (Simmons et al. 2010). However, a number of additional features are observed in the *LLNL-G3Dv1.0* model including deep slabs originating from the Japan subduction zone and detailed upper mantle structures beneath the Middle East region (see Figure 8).

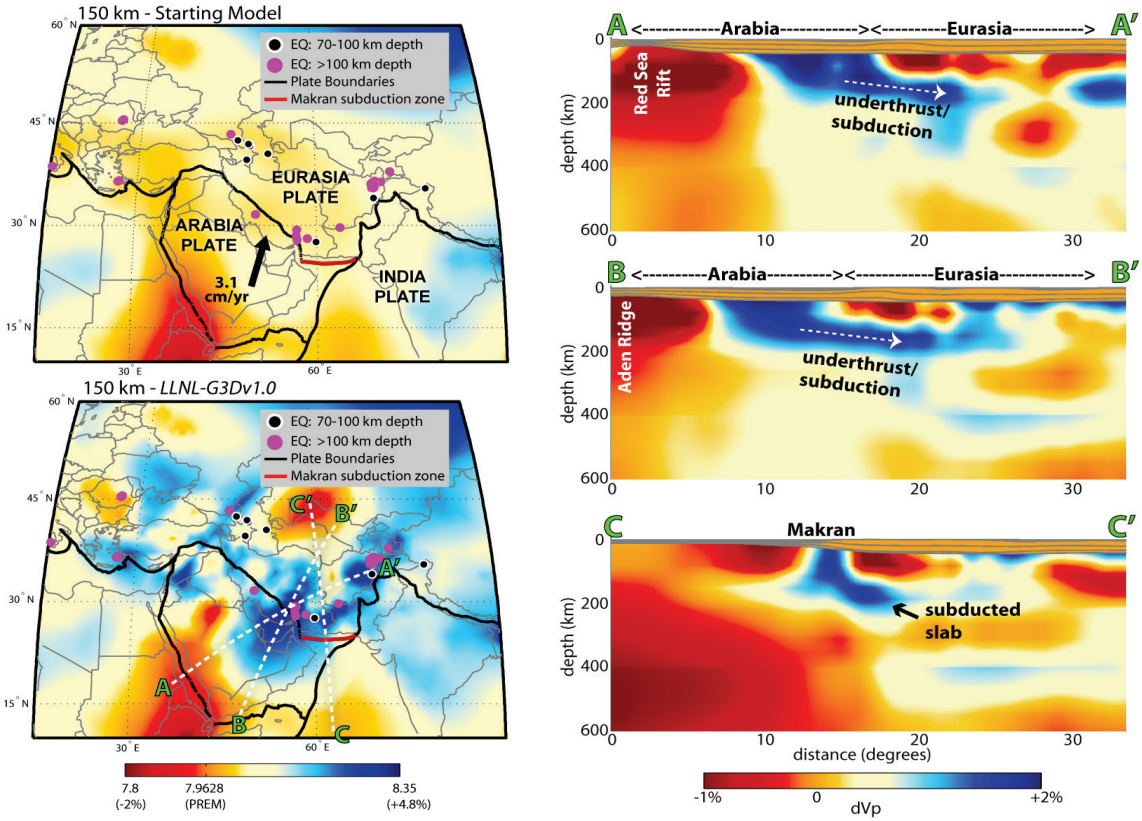

Figure 8. (left column) Close-up view of the *P* -wave velocity at 150 km depth from the *LLNL-G3Dv1.0* model. The final model differs dramatically from the starting solution in the shallow upper mantle beneath the Middle East region. Most notably, several high-velocity structures emerge beneath the region and correlate well with the location of deep earthquakes used in this study. (right column) Cross sections along the A-A', B-B' and C-C' transects. Velocity perturbations are relative to the global mean velocity anomalies in *LLNL-G3Dv1.0* at each depth. High-velocity structures extending from Arabia to beneath Eurasia represent underthrusted continental lithosphere along the western plate boundary and subducted oceanic lithosphere beneath the Makran region along the southern plate boundary.

CONCLUSIONS AND RECOMMENDATIONS

Our initial monitoring model, named *LLNL-G3Dv1.0*, is a global-scale tomographic model of *P* -wave velocity that predicts >800,000 *P* and >46,000 P_n travel times (mostly from Middle East events) to within 0.53 seconds standard deviation. The model is built with the tools and processes described in this report including: *BayesLoc* data processing, 3-D ray tracing with multi-pathing, and PMTI imaging. The current model consists of large-scale mantle structures such as spreading centers, cratons, superplumes and lower mantle slabs (generally observed in all modern global tomography models). In addition, the image depicts remarkably detailed structures in the upper mantle below the Middle East, owing to the dense data coverage in the region and data consistency yielded by the *BayesLoc* processing. In addition to predicting travel times, our model provides a new and important perspective of the upper mantle structures associated with convergence of the Arabia and India plates with Eurasia. In particular, we image the underthrusted continental Arabian lithosphere beneath Iran along the western Arabia-Eurasia plate boundary. In addition, the transition from continent-continent collision to subduction beneath the Makran region along the southern Arabia-Eurasia boundary is evidenced by the imaged structures in the *LLNL-G3Dv1.0* model. The next phase in this modeling effort will be to perform the same procedures described in the current study with a massive set of teleseismic *P* travel time data that are more globally distributed than the data considered herein. In conjunction, P_n travel time data from multiple regions will be considered simultaneously for the purpose of self-consistent travel time prediction at both regional and teleseismic distances.

REFERENCES

Antolik, M., G. Ekström and A. M. Dziewonski (2001), Global event location with full and sparse data sets using three-dimensional model of mantle *P* -wave velocity, *Pure Appl. Geophys*. 158: 291–317.

Antolik, M., Y. J. Gu, G. Ekström and A. M. Dziewonski (2003), J362D28: a new joint model of compressional and shear velocity in the Earth's mantle, *Geophys. J. Int*. 153: 443–466.

Ballard, S., J. Hipp, and C. Young (2008). Robust, extensible representation of complex Earth models for use in seismological software systems, in *Proceedings of the 30th Monitoring Research Review: Ground-Based Nuclear Explosion Monitoring Technologies*, LA-UR-08-05261, Vol. 1, pp. 347–355.

Ballard, S., J. R. Hipp and C. J. Young (2009), Efficient and accurate calculation of ray theory seismic travel time through variable resolution 3D Earth models, *Seis. Res. Lett*. 80(6): 990–1000.

Baumgardner, J. R. and P. O. Frederickson (1985), Icosahedral discretization of the two-sphere, *SIAM J. Numer. Anal*. 22(6): 1107–1115.

Chiao, L. -Y. and B. -Y. Kuo (2001), Multiscale seismic tomography, *Geophys. J. Int*., *145*, 517–527.

Constable, C. G., R. L. Parker and P. B. Stark (1993), Geomagnetic field models incorporating frozen-flux constraints, *Geophys. J. Int.* 113: 419–433.

Engdahl, E. R., R. van der Hilst and R. Buland (1998). Global teleseismic earthquake relocation with improved travel times and procedures for depth determination, *Bull. Seismol. Soc. Am*. 88(3): 722–743.

Ishii, M. and A. M. Dziewonski (2002). The innermost inner core of the Earth: Evidence for a change in anisotropic behavior at the radius of about 300 km, *PNAS*, 99(22): 14026–14030.

Kennett, B. L. N., E. R. Engdahl and R. Buland (1995). Constraints on seismic velocities in the Earth from travel times, *Geophys. J. Int*. 122: 108–124.

Myers, S. C., G. Johannesson and W. Hanley (2007). A Bayesian hierarchical method for multiple-event seismic location, *Geophys. J. Int*. 171: 1049–1063.

Myers, S. C., G. Johannesson and W. Hanley (2009). Incorporation of probabilistic seismic phase labels into a Bayesian multiple-event seismic locator, *Geophys. J. Int*. 177: 193–204.

Myers, S. C., M. L. Begnaud, S. Ballard, M. E. Pasyanos, W. S. Phillips, A. L. Ramirez, M. S. Antolik, K. D. Hutchenson, J. J. Dwyer, C. A. Rowe and G. S. Wagner (2010a). A crust and upper-mantle model of Eurasia and North Africa for P_n travel-time calculation, *Bull. Seismol. Soc. Am*. 100(2): 640–656.

Paige, C. C. and M. A. Saunders (1982), LSQR: an algorithm for sparse linear equations and sparse least squares, *ACM Transactions on Mathematical Software*, 8: 43–71.

Ritzwoller, M. H., N. M. Shapiro, A. L. Levshin, E. A. Bergman and E. R. Engdahl (2003). Ability of a global three-dimensional model to locate regional events, *J. Geophys. Res*. 108(B7): doi: 10.1029/2002JB002167.

Ruppert, S., D., Dodge, A. Elliott, M. Ganzberger, T. Hauk and E. Matzel (2005). Enhancing seismic calibration research through software automation and scientific information management, in *Proceedings of the 27th Seismic Research Review: Ground-Based Nuclear Explosion Monitoring Technologies,* LA-UR-05-6407, Vol. 2, pp. 937–945.

Sambridge, M. and R. Faletič (2003). Adaptive whole Earth tomography, *Geochem. Geophys. Geosys*. 4(3): doi:10.1029/2001GC000213.

Simmons, N. A., S. C. Myers and A. Ramirez (2009). Multi-resolution seismic tomography based on a recursive tessellation hierarchy, in *Proceedings of the 2009 Monitoring Research Review: Ground-Based Nuclear Explosion Monitoring Technologies*, LA-UR-09-05276, Vol. 1, pp. 211–220.

Simmons, N. A., A. M. Forte, L. Boschi and S. P. Grand (2010). GyPSuM: A joint tomographic model of mantle density and seismic wave speeds, *J. Geophys. Res*. (under review).

Um, J. and C. Thurber (1987). A fast algorithm for two-point seismic ray tracing, *Bull. Seismol. Soc. Am*. 77: 972–986.

Wang, Z. and F. A. Dahlen (1995). Spherical-spline parameterization of three-dimensional Earth models, *Geophys. Res. Lett*. 22(22): 3099–3102.

Yang, X., I. Bondár, J. Bhattacharyya, M. Ritzwoller, N. Shapiro, M. Antolik, G. Ekström, H. Israelsson and K. McLaughlin (2004). Validation of regional and teleseismic travel-time models by relocating ground-truth events, *Bull. Seismol. Soc. Am*. 94(3): 897–919.

Zhao, D., A. Hasegawa, and S. Horiuchi (1992). Tomographic imaging of *P* and *S* wave velocity structure beneath northeastern Japan, *J. Geophys. Res*. 97: 19909–19928.

Zhao, D. and J. Lei (2004). Seismic ray path variations in a 3D global velocity model, *Phys. Earth Planet. Int*. 141: 153–166.

Zhou, H. -W. (1996). A high-resolution *P* wave model for the top 1200 km of the mantle, *J. Geophys. Res.* 101(B12), 27791–27810.